Processing of a novel nanostructured ferritic steel via spark plasma sintering and investigation of its mechanical and microstructural characteristics

Somayeh Pasebani,[a,d] Indrajit Charit,[a,d] Yaqiao Wu,[b,d] Jatuporn Burns,[b,d] Kerry N. Allahar,[b,d] Darryl P. Butt[b,d] and James I. Cole[c,d]

[a] University of Idaho, Moscow, ID 83844-3024, United States
[b] Boise State University, Boise, ID 83427, United States
[c] Idaho National Laboratory, Idaho Falls, ID 83401, United States
[d] Center for Advanced Energy Studies, Idaho Falls, ID 83401, United States

Abstract

Nanostructured ferritic steels (NFSs) with 12-14 wt% Cr have attracted widespread interest for potential high temperature structural and fuel cladding applications in advanced nuclear reactors. They have excellent high temperature mechanical properties and high resistance to radiation-induced damage. The properties of the NFSs depend on the composition that mainly consists of Cr, Ti, W or Mo, and Y_2O_3 as alloying constituents. In this study, a novel nanostructured ferritic steel (Fe-14Cr-1Ti-0.3Mo-0.5La_2O_3, wt%) termed as 14LMT was developed via high energy ball milling and spark plasma sintering. Vickers microhardness values were measured. Microstructural studies of the developed NFSs were performed by EBSD and TEM, which revealed a bimodal grain size distribution. A significant number density of nano-precipitates was observed in the microstructure. The diameter of the precipitates varied between 2-70 nm and the morphology from the spherical to faceted shape. The Cr-La-Ti-O-enriched nanoclusters were identified by APT studies.

Introduction

Nanostructured ferritic steels (NFSs) have attracted considerable interest for potential use in fuel cladding and other structural applications. These steels possess enhanced microstructural stability, high creep strength and excellent radiation damage tolerance [1,2]. The unique properties of NFSs such as 14YWT derive from the presence of an ultrahigh number density of Y-Ti-O-rich nanoclusters. These nanoclusters are formed due to the mechanical alloying (MA) of Fe-Cr-Ti powders with yttria (Y_2O_3) followed by hot consolidation route [3,4]. The most commonly used rare earth (RE) oxide in the ferritic ODS or NFSs is Y_2O_3. In the present study, an alternative RE oxide, lanthana (La_2O_3) was added to the NFS composition instead of the traditionally used Y_2O_3. Lanthana is stable at high temperatures, insoluble in solid iron at all temperatures and has a high affinity for oxygen. Based on the density function theory calculations by Reed et al. [5], La_2O_3 clusters should have the same general structure as the corresponding yttrium species; however, the bond distances are generally greater. Furthermore, La_2O_3 is more abundant (25-38 wt%) in one of the main US rare earth ores (bastnasite) compared with Y_2O_3 (only about 0.2 wt%). There is no study in the literature on dispersing La_2O_3 to the bulk ferritic matrix to the best of our knowledge. Interestingly, Mueller et al. [6] investigated the oxide dispersion strengthening effect of La_2O_3, Y_2O_3 and ZrO_2 in Mo and found that La_2O_3 doping produced the highest ultimate tensile strength (UTS) and significantly higher creep-

rupture properties compared to the other dopant oxides. Thus, an alloy with the nominal composition of Fe-14Cr-1Ti-0.3Mo-0.5La_2O_3 (wt%), termed 14LMT, has been developed using MA of the constituent powders. A detailed study on the microstructural characteristics of the as-milled 14LMT powder as a function of various MA parameters was carried out by Pasebani et al. [7].

Generally, NFSs are produced via the mechanical alloying followed by the hot consolidation process such as the hot isostatic pressing (HIP) and/or hot extrusion. In this study, such traditional consolidation methods of producing NFSs were replaced by a relatively new technique called spark plasma sintering (SPS). Compared to the hot pressing and HIP, the SPS technique allows sintering at lower temperatures and shorter dwell times. In SPS, the powder mix is placed in a graphite die before being pressed and a DC pulsed voltage is applied to the compact. In the case of electrically conductive materials, the heating is mainly due to the Joule effect. Although the occurrence of the electrical discharge (plasma discharge) is widely mentioned in the literature, its existence has not been conclusively proved. Several other phenomena, such as local melting, surface and volume diffusion and the evaporation of oxide layers, enhance the formation of necks between the powder particles leading to final densification [8].

Heintze et al. [9,10] consolidated the ODS Fe-9Cr model alloys, Fe-9Cr, Fe-9Cr-0.3Y_2O_3 and Fe-9Cr-0.6Y_2O_3 (wt%), using SPS and studied the mechanical properties as well as microstructural characteristics of the alloys. The hardness values for the Fe-9Cr ODS alloys containing 0.3 wt% and 0.6 wt% Y_2O_3 were in the range of 216-322 HV depending on the milling time and initial powder size. Recently, Allahar et al. [11] used SPS to consolidate the Fe-16Cr-3Al (wt%) powder with sequential additions of Y_2O_3 and Ti powders to produce Fe-16Cr-3Al-0.5Y_2O_3 (wt%) and Fe-16Cr-3Al-0.5Y_2O_3-1Ti (wt%) alloys, respectively. The hardness values of the alloys increased to 320-400 and 480 HV after adding 0.5Y_2O_3 and 0.5Y_2O_3-1Ti to the Fe-16Cr-3Al matrix, respectively. The microstructure of the consolidated ODS alloys contained both ultrafine and coarse grains attributed to the occurrence of recrystallisation during SPS at 1 000°C. The TEM and APT studies revealed Y-O and Y-Ti-O-enriched nanoclusters with Y:O:Ti ratio of 3:10:8 and M:O (metal to oxygen) ratio close to 1:1, which were similar to those obtained in NFSs sintered by other hot consolidation methods.

A preliminary investigation [12] on the MAed 14LMT powder revealed nanoclusters in the nanocrystalline ferritic matrix. Subsequently, a detailed study on the MAed 14LMT powder was carried out as a function of MA parameters [7], and the formation of Cr-Ti-La-O-enriched nanoclusters during MA was identified. The present study focuses on the consolidation of the MAed 14LMT powder via SPS. Further, it elucidates the effects of SPS parameters such as temperature, dwell time, heating rate, applied pressure and current, on the density, microstructure and mechanical properties of the 14LMT alloy.

Experimental

The starting constituent powders including Fe (99.9 wt% Fe, average particle size of 40 µm), Cr (99.8 wt%, average particle size of 5 µm), Ti (99.7 wt% Ti, average particle size of 26 µm), La_2O_3 (99.99 wt% La_2O_3, average particle size of 40 nm) and Mo (99.9 wt% Mo, average particle size of 1-2 µm) were mixed together in the nominal proportion of Fe-14Cr-1Ti-0.3Mo-0.5La_2O_3 (wt%). High energy ball milling was performed in an air-cooled SPEX 8000M shaker mill for 10 h using steel balls (8 mm in diameter) as the milling media and the ball to powder ratio (BPR) of 10:1 (here 100 g steel balls were used for milling of 10 g powder mixture in each milling batch).

A Dr. Sinter Lab SPS-515S machine (SPS Syntex Inc., Kanagawa, Japan) available at the Center for Advanced Energy Studies (CAES) was used to consolidate the as-milled powder. A Tri-Gemini cylindrical graphite die with an inner diameter of 12.7 mm and an outer diameter of 38 mm was used. The inner surface of the die was covered with a graphite foil with a thickness of 0.25 mm to facilitate sample removal. In order to inhibit the diffusion of carbon from the graphite foil, a thin niobium foil was placed between the

powder and the graphite foils. The die was wrapped in a layer (4 mm thickness) of graphite felt to minimise heat loss by thermal radiation.

The as-milled powder was sintered under vacuum (7×10^{-3} Torr) at different temperatures (850-1 100°C) for various dwell times (0, 2, 20 and 45 min) using the pulse pattern 12-2 (the cycle consisted of 12 ms current passage followed by no current for 2 ms), a heating rate of 100°C/min, and a pressure of 80 MPa. The dwell time of "0 min" implies that the powder was essentially heated and cooled without any isothermal holding. The applied pressure and the heating rate were also varied between 40-110 MPa and 50-200°C/min, respectively, at a constant temperature of 950°C and a dwell time of 7 min. To investigate the effect of pulsed current, the average electric current was decreased from 275 A (in normal condition) to 150 A by placing a non-conductive ceramic disk between the punch and the powder.

The density of the sintered specimens was measured by Archimedes' method. At least six measurements were made for each specimen. The final relative density was determined as the ratio between the measured and the theoretical density (~7.7 g/cm^3). The Vickers microhardness tests were performed with a Leco LM100 microhardness tester at a 1 000 g-f (9.81 N) with a dwell time of 15 s.

Microstructural characteristics of the sintered specimens were examined using a LEO Supra 35 VP FESEM at an accelerating voltage of 15-20 kV. Some specimens were also prepared for electron back-scatter diffraction (EBSD) characterisation by grinding on 120 to 1 200 grit SiC papers, followed by a final polish in a Buehler Vibromet-2 vibratory polisher using 0.05 µm alumina slurry for 6 to 24 h. The EBSD analysis was performed on a JEOL JSM-6610LV scanning electron microscope (SEM) equipped with an EDAX/TSL Hikari EBSD system. The SEM was operated at an accelerating voltage of 20 kV. The automated scan was performed with a 0.1 µm step size on a total area of 50×50 µm^2. The EBSD data were analysed using the TSL Orientation Imaging Microscopy (OIM™) Data Collection version 5.31 software. After SPS, disks of 3 mm in diameter were mechanically thinned, and electropolished in CH_3OH-HNO_3 (80:20 by vol.%) electrolyte at -40°C using a Fischione Model 110 Twin-Jet Electropolisher. Transmission electron microscopy (TEM) studies along with the energy dispersive spectroscopy (EDS) were performed using a FEI Tecnai TF30-FEG STEM operated at 300 kV.

A focused ion beam (FIB) was used to prepare specimens for the atom probe tomography (APT) studies. The FIB effort was carried out using a Quanta 3D FEG instrument with a Ga-ion source. The APT analysis carried out using an Imago LEAP 4000X HR operating in voltage mode at the specimen temperature of 50–60 K and 20% of the standing voltage pulse fraction. The atom maps were reconstructed using CAMECA IVAS 3.6 software. The method followed here for the cluster analysis was described by Miller et al. [13] and Williams et al. (2013) [14].

Results and discussion

Effects of SPS temperature and time on densification and mechanical properties

The sintering experiments were performed in the temperature range of 850-1 100°C for dwell times of 0 and 2 min at a constant heating rate of 100°C/min and an applied pressure of 80 MPa. The measured density values are plotted as a function of sintering temperatures for the dwell times of 0 (i.e., no dwelling) and 2 min, and designated as plot-1 and plot-2, respectively, in Figure 1. The relative density values in the plot-1 of Figure 1 increased with increasing SPS temperatures from 850 to 1 100°C, with significant increase from 89.5% at 900°C to 97% at 950°C and only a slight increase at temperatures above 950°C. The relative density of 98.5% was achieved at 1 100°C. Similarly, the relative density values in plot-2 of Figure 1 increased with increasing dwell time from 0 to 2 min at temperatures below 950°C and did not show significant difference with increasing dwell time from 0 to 2 min at temperatures above 950°C.

Figure 1: The variation of relative density and microhardness as a function of SPS temperature

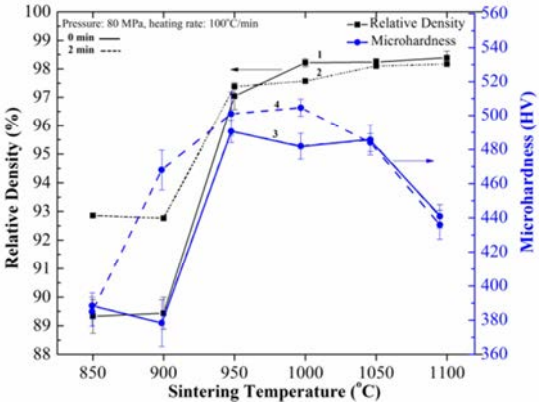

The microhardness values for dwell times of 0 and 2 min are presented in the plot-3 and plot-4 of Figure 1, respectively. The microhardness values shown in plot-3 of Figure 1 progressively increased from 388.5 HV at 850°C to 490.6 HV at 950°C and remained unchanged up to 1 050°C and decreased down to 441 HV at 1 100°C. The microhardness values shown in plot-4 of Figure 1 were consistently higher for the dwell time of 2 min than the dwell time of 0 min at SPS temperatures below 1 000°C. The relative density and microhardness data for 2 min dwell time (Figure 1 – plot 2 and 4) clarified three distinct stages of the sintering process as a function of SPS temperature (850-1 100°C). In the temperature range of 850-900°C, significant hardening occurred without much improvement in densification; at 900-1 000°C both densification and hardening occurred; and above 1 000°C the extent of densification did not change much at all but microhardness was found to be less. It can be argued that at temperatures higher than 1 000°C the microhardness values dropped because of the microstructural evolution possibly due to coarsening of grains and oxide precipitates.

Figure 2: Influence of sintering time on (a) the relative density and (b) microhardness, at SPS temperatures at 850, 950 and 1 050°C

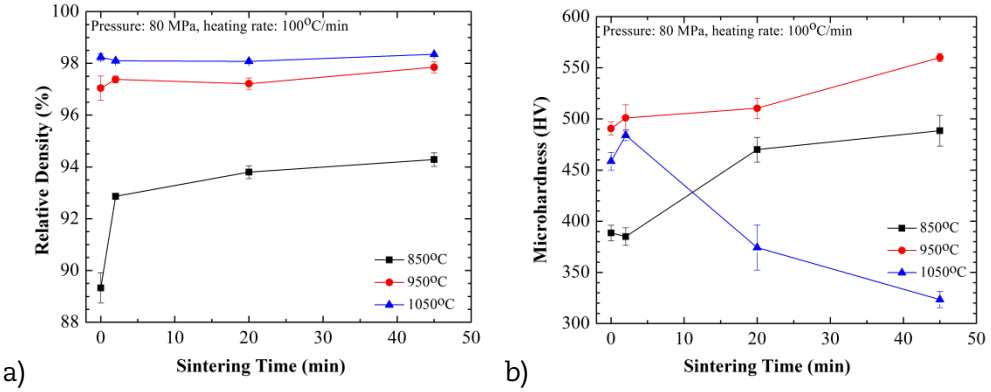

In order to understand the effect of SPS temperature and time, three temperatures (850, 950 and 1 050°C) were selected from Figure 1 and the dwell time was varied between 0 and 45 min at those three temperatures. The density and microhardness were measured and presented in Figure 2a and b, respectively. The relative density of the SPSed specimens increased with increasing SPS temperatures between 850-1 050°C at all dwell times. The microhardness values of the 14LMT alloys SPSed at 850 and 950°C increased consistently with increasing dwell time from 0 to 45 min. However, the microhardness showed a decrease at 1 050°C after 2 min. The microhardness values were 488.5, 591 and 323.5 HV, after SPS at 850, 950 and 1 050°C for 45 min, respectively.

Effect of SPS temperatures and times on the microstructural evolution

SEM and EBSD studies

The SEM micrographs along with corresponding EBSD maps as insets from various 14LMT alloy specimens SPSed at different temperatures for a dwell time of 45 min are shown in Figures 3a-c. A bimodal grain size distribution (nano grains and coarse grains) was observed in all the micrographs and the volume fraction of the coarse grains increased with higher SPS temperatures. Some remained porosity is observed as black regions in the back scattered SEM and EBSD micrographs shown in Figures 3a-c. The area fraction of porosity in the 14LMT alloy SPSed significantly decreased with increasing sintering temperature from 850°C to 950°C. The area fraction of porosity was estimated to be 5.1%, 2.1% and 1.0% at SPS temperature of 850, 950 and 1 050°C, respectively. Grain coarsening occurred with increasing SPS temperature up to 1 050°C as shown in Figure 3c.

Figure 3: SEM and EBSD micrographs of the specimens SPSed for 45 min at (a) 850°C, (b) 950°C, (c) 1 050°C (Note that the inset EBSD microgarphs have a marker scale of 10 µm in length)

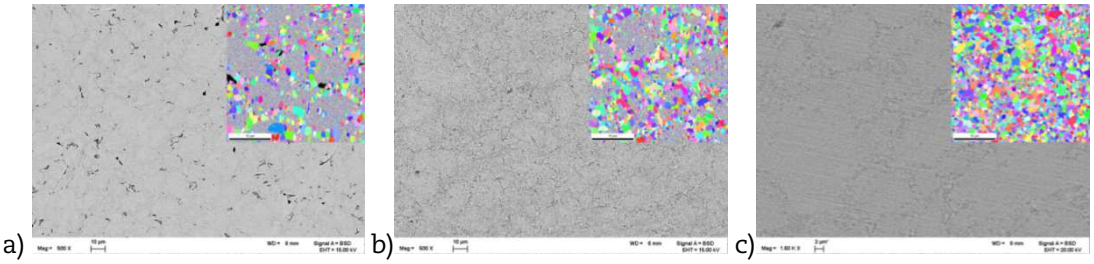

TEM studies

The TEM study was focused on the 14LMT alloy SPSed at 950°C for 45 min. In Figure 4a, an example of the bimodal grain size distribution showed that the ultrafine grains were surrounded by nanograins, and a high number density of the nano-precipitates in both types of grains. A high density of dislocations and nano-precipitates interacting in a grain interior with an average diameter of 1 µm has been shown in Figure 4b. In the vicinity of this micron-sized grain there were nanograins, and dislocation densities in the fine ferrite grains were higher than in the coarse grains as shown in Figure 4c. It has been noticed that in the micron-sized grains the precipitates were larger and/or located at the grain boundaries where as in the nanograins, precipitates were smaller and located inside the grains. A high angle annular dark field (HAADF) STEM micrograph of the sintered 14LMT alloy is shown in Figure 4d.

Nano-precipitates with different Z-contrast could be distinguished from the bcc ferritic matrix as the contrast of these precipitates was due to a difference in their chemical compositions as compared to that of the matrix. Several EDS analyses on a large area located in the matrix revealed a chemical composition of Fe-1.4Ti-15.19Cr-0.23Mo-0.55La (wt%) that was close to the nominal composition. Larger and smaller precipitates were observed along the grain boundaries and in the grain interiors, respectively. Two different types of the precipitates were observed in the HAADF micrograph; the nano precipitates with a darker contrast, spherical morphology and average size varying from 20 to 50 nm (mostly located at the grain boundaries), and the nano-precipitates with a brighter contrast, faceted morphology and average size varying from 2 to 30 nm (mostly located in the grain interior).

Figure 4: TEM micrographs of the specimen SPSed at 950°C for 45 min
a) Bright field micrograph of micron-sized and nanograins
b) a larger grain with high dislocation and precipitate density
c) nanograined region of the microstructure
d) STEM-HAADF image showing the distribution of the nano-precipitates

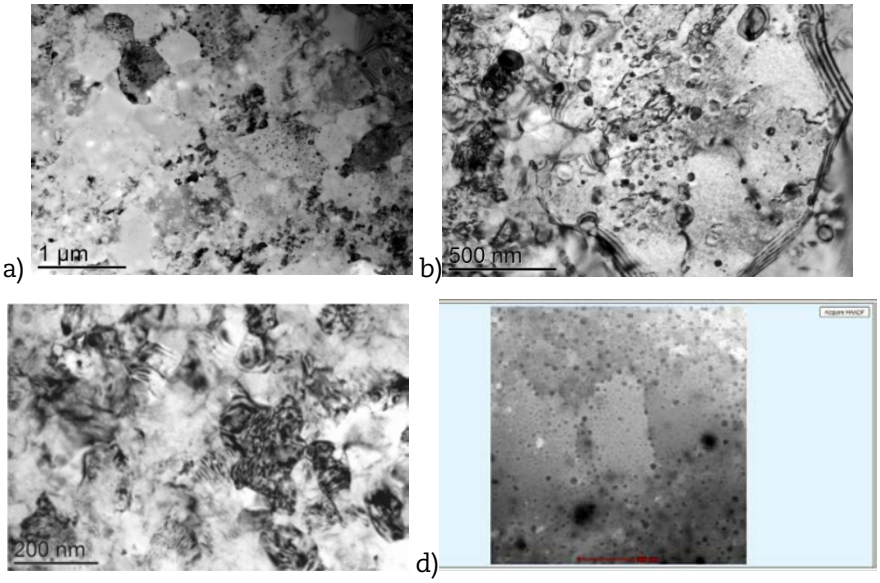

APT studies

Figure 5 illustrates the location of different species (CrO, O, Mo, Ti, TiO, La and LaO) in the APT reconstruction maps of the 14LMT alloy SPSed at 950°C for 45 min. The region sampled in the APT experiment corresponds to the TEM BF image presented prior to the APT maps in Figure 5. A uniform clustering of CrO, TiO, La and O is clearly evident in the APT maps. This was also confirmed by the TEM BF and HAADF micrographs taken from the tip prior to the APT experiment. Such nanoclusters were also noted in the MAed powder as discussed elsewhere [7]. The number density of CrO-TiO-La-enriched nanoclusters in 14LMT alloy SPSed at 950°C for 45 min was estimated to be 1.2×10^{24} m^{-3} with the average Guinier radius of 1.5±0.3 nm. The average cluster composition 8.9 at.% Cr, 17.8 at.% Ti and 5.9 at.% La, 35.6 at.% O along with Fe as the balance. Based on the matrix-corrected cluster composition, the ratio of Cr:Ti:La:O was found to be 4:3:1:5.

Figure 5: A bright field TEM image of an 14LMT (950°C and 45 min) APT specimen prior to analysis (on the top left) and 3-D APT reconstruction maps obtained from the same tip

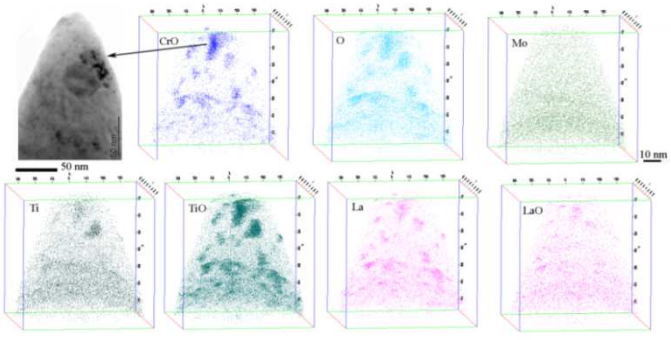

The number density of CrO-TiO-La-enriched nanoclusters in 14LMT alloy SPSed at 950°C for 45 min was estimated to be 1.2×10^{24} m^{-3} with the average Guinier radius of 1.5±0.3 nm. The average cluster composition 8.9Cr-17.8Ti-5.9La-35.6O (at%) along with Fe

as the balance. Based on the matrix-corrected cluster composition, the ratio of Cr:Ti:La:O was found to be 4:3:1:5. Miller et al. [15] a high number density (2×10^{24} m^{-3}) of ultrafine Ti-Y-O-enriched particles with an average Guinier radius of 1.2±0.4 nm in the MA957 ODS alloy. The composition of these particles was estimated by the envelope method to be Fe-(32.9±5.3)Ti-(15.4±7.3)Y-(39.9±6.9)O-(1.7±1.7)Cr-(0.02±0.2)Mo (at%). To study the effect of SPS temperatures on the nanocluster size, distribution and chemical composition, similar APT analysis (not shown here) was carried out on the 14LMT alloy SPSed at 1 050°C for 45 min. Clustering of CrO, TiO and La was clearly observed. The number density of CrO-TiO-La-enriched nanoclusters in the sample consolidated at 1 050°C was estimated to be 0.66×10^{24} m^{-3} with the average Guinier radius of 1.8±0.4 nm. With increasing SPS temperature from 950 to 1 050°C, the number density of nanoclusters decreased whereas the Guinier radius increased. However, the change is found to be minimal. For the oxide precipitates, the concentration ratio of Cr:Ti:La:O was calculated to be about 2:2:4:1 based on the matrix-corrected composition.

Effect of heating rate, applied pressure and pulsed electric current

The relative density and microhardness values for the 14LMT specimens SPSed with various heating rates, applied pressures and pulsed electric currents is summarised in Table 1. The SPS temperature and dwell time was kept at 950°C and 7 min, respectively. The relative density values increased slightly with increasing heating rates from 50 to 200°C/min, which is likely due to a large thermal gradient existing with higher heating rates.

Table 1: Relative density and microhardness for various heating rates, applied pressures and pulsed electric currents (the SPS temperature and dwell time were 950°C and 7 min)

SPS parameter		Relative density (%)	Microhardness (HV)
Heating rate (°C/min)	50	97.75±0.06	513.5±5.3
	100	97.87±0.04	492.7±7.8
	150	98.27±0.06	505.4±10.8
	200	98.40±0.02	482.0±6.4
Applied pressure (MPa)	40	90.76±0.04	300.3±13.3
	60	97.06±0.08	462.2±12.2
	80	97.87±0.04	492.7±7.8
	90	98.11±0.08	533.0±6.5
	110	98.30±.08	549.0±9.5
Pulsed electric current (A)	150	96.18±0.08	447.4±23.1
	275	97.87±0.04	492.7±7.8

The microhardness values slightly decreased with increasing heating rate from 50 to 200°C/min except an increase from 100 to 150°C/min. This higher microhardness values at a lower heating rate might have been caused by a greater oxygen pickup during heating or larger number density of the nano-precipitates and subgrains because of longer provided time for diffusion-based processes such as grain boundary diffusion or surface diffusion. Li et al. [16] have shown that the use of a high heating rate ensures oxide-free, well-sintered clean interfaces between powder particles in contrast to oxide-enveloped, poorly-sintered interfaces achieved with a slow heating rate. However, investigations on the effect of heating rate on densification in the SPSed products have shown conflicting results. For example, the heating rate (between 50 to 700°C/min) had no effects on the density of alumina (non-conductive) and $MoSi_2$ (with a good conductivity) [17,18]. Higher densification has been achieved by increasing the applied pressure from 40 to 110 MPa with a significant rate of increase from 40 to 60 MPa.

The pulsed electric current was decreased from 275 A (in normal condition) to 150 A. The pulse pattern of 12-2 was used in this study. However, the pulse pattern has no or little influence on the grain size and density according to the literature. Although higher density and microhardness were achieved at the higher SPS current, but the difference was not significant. Munir et al. [18] noted that during SPS the current and temperature are dependent variables and their influence cannot be clearly separated. During SPS, the powder is heated by Joule heating by the applied current passing through it. In addition to direct heating role of the DC current, the mass transfer can be enhanced at higher currents due to the increase in concentration of defects and mobility of the defects [18]. Thus, a higher density and hardness could be achieved at higher current levels.

Conclusions

A novel class of NFSs (14LMT alloys) was developed using La_2O_3 as an alternative RE addition via a processing route combining the mechanical alloying and spark plasma sintering techniques [19]. The relative density and hardness increases as a function of temperature and time, but at the sintering temperature of 1 050°C, the hardness decreased presumably due to the coarsening of the grains and some of the oxide precipitates. The optimum hardness and density was obtained at a SPS temperature of 950°C and 45 min. The microstructures of the 14LMT alloys were studied by SEM-EBSD, TEM and APT. The EBSD studies revealed the development of a bimodal grain size distribution via the dynamic recrystallisation process. The particle size and morphology were investigated by TEM and revealed a size range of 2-70 nm. The APT experiments revealed Cr-La-Ti-O based nanoclusters in SPSed 14LMT alloys. The lower heating rates provided higher microhardness values but lower density. Higher density and hardness values were achieved at higher applied pressure and pulsed electrical current. While further work is needed, this study demonstrates that the lanthana addition and SPS could provide novel approaches of alloy design and processing for developing NFSs.

Acknowledgements

This work was supported partly by the Laboratory Directed Research and Development Program of Idaho National Laboratory, Contract DE-AC07-05ID14517, and partly by a grant of the Advanced Test Reactor National Scientific User Facility (ATR NSUF).

References

[1] Odette, G.R., M.L. Alinger, B.D. Wirth (2008), "Recent developments in irradiation-resistant steels", Annu. Rev. Mater. Res., 38, pp. 471-503.

[2] Wu, Y. et al. (2012), "Transmission electron microscopy characterisation of the nanofeatures in nanostructured ferritic alloy MA957", *Acta Materialia*, 60[8], pp. 3456-3468.

[3] Ukai, S., M. Fujiwara (2002), "Perspective of ODS alloys application in nuclear environments", Journa of Nuclear Materials, 307–311, pp. 749-757.

[4] Williams, C.A. et al. (2013), "The formation and evolution of oxide particles in oxide-dispersion-strengthened ferritic steels during processing", Acta Materialia, 61[6], pp. 2219-2235.

[5] Reed, Z.D., M.A. Duncan (2008), "Photodissociation of yttrium and lanthanum oxide cluster cations", Journal of Physical Chemistry, 112, pp. 5354-5362.

[6] Mueller, A.J. et al. (2000) "Evaluation of oxide dispersion strengthened (ODS) molybdenum and molybdenum-rhenium alloys", International Journal of Refractory Metals and Hard Materials, 18, pp. 205-2011.

[7] Pasebani, S. et al. (2013-I), "Mechanial alloying of lanthana-bearing nanostructured ferritic steel", Acta Materialia, 61[15], pp. 5605-5617.

[8] Gendre, M. et al. (2010), "A study of the densification mechanisms during spark plasma sintering of zirconium (oxy-)carbide powders", Acta Materialia, 58[7], pp. 2598-2609.

[9] Heintze, C. et al. (2011), "Microstructure of oxide dispersion strengthened Eurofer and iron–chromium alloys investigated by means of small-angle neutron scattering and transmission electron microscopy", Journal of Nuclear Materials, 2011. **416**(1–2): pp. 35-39.

[10] Heintze, C. et al. (2012), "Nanoscale characterisation of ODS Fe–9%Cr model alloys compacted by spark plasma sintering", Journal of Nuclear Materials, 428, pp. 139-146.

[11] Allahar, K.N. et al. (2013), "Ferritic oxide dispersion strengthened alloys by spark plasma sintering", Journal of Nuclear Materials, 443[1–3], pp. 256-265.

[12] Pasebani, S. et al. (2013-II), "A preliminary study on the development of La_2O_3-bearing nanostructured ferritic steels via high energy ball milling", Journal of Nuclear Materials, 434[1-3], pp. 282-286.

[13] Miller, M.K. (2000), Atom probe tomography, Kluwer Academic/Plenum, New York.

[14] Williams, C.A. et al. (2010), "Nanoscale characterisation of ODS–Eurofer 97 steel: An atom-probe tomography study", Journal of Nuclear Materials, 400[1], pp. 37-45.

[15] Miller, M.K. et al. (2004), "Nanometer scale precipitation in ferritic MA/ODS alloy MA957", Journal of Nuclear Materials, 329–333, pp. 338-341.

[16] Li, X.P. et al. (2013), "The critical role of heating rate in enabling the removal of surface oxide films during spark plasma sintering of Al-based bulk metallic glass powder", Journal of Non-Crystalline Solids, 375, pp. 95-98.

[17] Stanciu, L.A. et al. (2001), "Effects of heating rate on densification and grain growth during field assisted sintering of α-Al_2O_3 and $MoSi_2$ powders", Metallurgical and Materials Transactions A, 32A, pp. 2633-2638.

[18] Munir, Z.A. et al. (2006), "The effect of electric field and pressure on the synthesis and consolidation of materials: A review of the spark plasma sintering method", Journal of Materials Science, Vol. 41, No. 3, pp. 763–777, 2006.

[19] Shen, Z. et al. (2002), "Spark plasma sintering of alumina", Journal of the American Ceramic Society, 85, pp. 1921-1927.